Banner appropriate to article type will appear here in typeset article

arXiv:2611.14235v1 [cond-mat.soft] 10 Nov 2026

Banding instabilities in poroelastic media under flow-driven compaction

Joseph J. Webber†

Mathematics Institute, University of Warwick, Coventry CV4 7AL, UK

(Received xx; revised xx; accepted xx)

When cross-linked poroelastic media are subjected to a hydrostatic pressure difference, they compact, remaining fully swollen on their uppermost surface and becoming increasingly compressed with depth. A critical unexplored effect of cross-linking and resistance to shear deformation is investigated, which is not seen in classical models of poroelastic media treated as free elastic spheres, and resists the kind of compressive compaction that characterises these systems. Eventually, a steady-state profile dependent on osmotic, shear and transport properties is reached, supporting a uniform interstitial flow wherein the medium acts like a passive filter. In this paper, we show how these steady-state profiles are not necessarily stable, and propose a mechanism for the formation of instabilities, wherein some regions of the medium swell and others compact, forming distinctive horizontal or vertical banding patterns. In the latter case, these bands appear qualitatively to be higher-permeability conduits or channels, similar to wormholes or tunnels seen in granular media. It is possible to quantify the effect of changing the pressure head on the growth rate of instabilities and the separation lengthscale in this channelisation case, and how material properties like shear stiffness and dependence of permeability on porosity affect the dynamics of instability. Critically, it is shown that these instabilities are a fluid-mechanical effect, with an entirely new mechanism based on the porosity–permeability relationship and not on elastic effects. With an understanding of these mechanisms, we can derive insight into channelisation in poroelastic systems in geophysics, human biology and industry.

Key words: Authors should not enter keywords on the manuscript, as these must be chosen by the author during the online submission process and will then be added during the typesetting process (see Keyword PDF for the full list). Other classifications will be added at the same time.

1. Introduction

A surprising variety of everyday situations can be reduced in effect to a case of fluid flow, driven by a pressure difference, across a soft porous material. Examples include flow through soft filters (Dhopeshwarkar *et al.* 2008; Song *et al.* 2019), the compaction of boluses in the intestines (Lentle *et al.* 2009) and fluid-filled structures like cartilage in joints (Lu

† Email address for correspondence: joe.webber@warwick.ac.uk

Abstract must not spill onto p.2

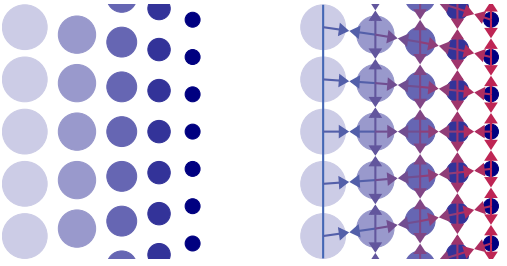


Figure 1: Poroelastic systems with no cross-linking can support arbitrary gradients in swelling state without the formation of large deviatoric stresses. When there is cross-linking, the second panel shows how a gradient in swelling state creates significant stresses in the matrix. In the absence of constraints, it may be favourable to relieve these stresses to lower the elastic potential energy of the system.

& Mow 2008; Godard *et al.* 2025). Indeed, even the high-pressure flow of near-boiling water through coffee grounds in espresso machines can be viewed as a pressure-driven poroelastic compaction problem (Waszkiewicz *et al.* 2025), even though the granules may be better viewed as a granular medium with only limited contributions from elasticity. Properly understanding these flows is also vital for a range of industrial applications, from paper manufacture (wood pulp compression prior to the drying of fibre mats) to hydraulic fracturing for petrochemical recovery (MacMinn *et al.* 2015; Paterson *et al.* 2019).

When a pressure difference can both drive a flow through a material and deform it, models need to capture a variety of effects from fluid and solid mechanics; such an example is described by Hewitt *et al.* (2016), who developed a uniaxial theory for compression of a porous layer formed from disjoint deformable spheres. Rich dynamics arise from the fact that fluid transport itself changes the transport properties of the medium, namely by compressing the solid matrix such that its permeability to flow decreases. Therefore, though increasing the hydrostatic pressure head across the layer initially increases the Darcy flux through the gel, this flux plateaus eventually when large pressure differences compress the layer so much that it is no longer sufficiently permeable to allow fluxes to grow unboundedly. More recent work (Bouckley *et al.* 2025) has considered pre-strained media and the effects of changing flow direction for different constitutive laws, illustrating how the steady-state compaction profiles that result from such processes can be highly non-trivial and dependent on a range of both material (e.g. elastic moduli and permeability) and situational (e.g. the geometry and pressure driving the flow) parameters. In certain circumstances, especially when the material is weakened by chemical effects, flow-induced compaction can result in pore closure, rendering the layer impermeable to flow if the applied pressure head is large enough (MacMinn *et al.* 2016; Ghosh *et al.* 2026).

In theoretical models, compaction is usually considered to be uniaxial, with stresses a function solely of solid fraction and shear effects neglected. In effect, this implies that the local stresses are entirely a function of local swelling state and not dependent on the state of the material as a whole. This is entirely reasonable in applications such as very soft solids or 'incoherent' materials like granular media or soils, like the situation pictured in panel (a) of figure 1 where solids can be treated as free particles. In cross-linked media like some hydrogels, however, any anisotropic deformation generates shear stresses as a result of the cross-linked polymer matrix (Webber & Worster 2023), and this has a significant effect on

the qualitative nature of the compressed gel layer when a fluid flow is driven through it. Though increased resistance to deformation drives faster interstitial flows (Biot 1941), it also resists compaction, and this effect (pictured in figure 1(b)) is investigated in detail in the present study: not only does the pressure drop across the layer have to balance stress due to local isotropic compaction, but also on gradients in compaction that generate shear stresses. This is investigated in the simplest case of flow-induced compaction of a poroelastic layer with the inclusion of shear effects in section 2, where the isotropic effective stress on the matrix is set using a simple expression for the (generalised) osmotic pressure (Peppin *et al.* 2005) that captures a maximum solid fraction beyond which no more water can be expelled (Webber & Worster 2025). Furthermore, different poroelastic media have potentially wildly different relationships between porosity and permeability, which can again lead to an array of compaction profiles.

Driving fluid flow through poroelastic beds is known to result in a channelling behaviour in certain circumstances, especially in the extraction process during coffee brewing (Lee *et al.* 2023), where channelling is a well-known problem resulting in poorer-quality coffee. The extreme pressures under which saturated coffee grounds can be placed during the brewing process leave very little space for fluid transport, and so high-pressure water can displace granules and form high-conductivity channels, within which there is very little contact between water and coffee. Morphologically such processes are akin to both wormhole formation in granular beds (Morgan *et al.* 2025) (a flow-rate-dependent result of driving fluid through packed beads in a Hele-Shaw cell), and dissolution-driven tunnelling that occurs in porous media when conductive pathways for water are created by the acid dissolution of carbonate rocks (Golfier *et al.* 2002). The mechanisms for such processes typically involve advection or dissolution of solid particles with the flow.

Considering cross-linked elastic media like gels, however, all deformation is reversible and there is no phase of the material that can be destroyed, nor can the scaffold be arbitrarily deformed out of place, right up to the point of fracture. Therefore, if channelisation is to occur in a qualitatively similar manner to in granular beds, an entirely different mechanism must be the driver. In this study, we propose that channelisation can be explained as a poroelastic instability of the compacted base state, driven by a permeability that reduces with compaction, and 'shields' the bulk of the gel layer from pressure differences, allowing for reswelling. This mechanism is potentially enhanced by the relief of deviatoric stresses in the bulk through growing an unstable state where deformation is closer to the ideal state of local isotropy.

In section 3, we study the linear stability of the compacted steady-state profiles computed in section 2. It is apparent that 'banding' patterns can form where interior regions of the medium swell and the surface region compacts, in a manner entirely independent of horizontal position. Section 4 uses this stability analysis to deduce the qualitative nature of these instabilities. At low pressures, the effect of anchoring from the base of the gel resists the formation of these horizontal banding instabilities, but it is shown that finite-wavenumber instabilities that take the form of "vertical channels" may be unstable in such a case. This provides a mechanism for the formation of channels; where regional deswelling shields other areas of the poroelastic medium and allows for reswelling – tempered by the diffusive tendency to drive flows from more swollen regions to less swollen areas and the effects of a fixed base. Together, these two effects lead to a most unstable wavenumber for the initially linear disturbance, setting a separation lengthscale between adjacent channels. The effect of material parameters on the growth rate and nature of these two distinct kinds of instability can then be studied, allowing us to propose an entirely novel poroelastic mechanism for such deformation, completely distinct from the channelisation processes that form qualitatively similar structures in granular media.

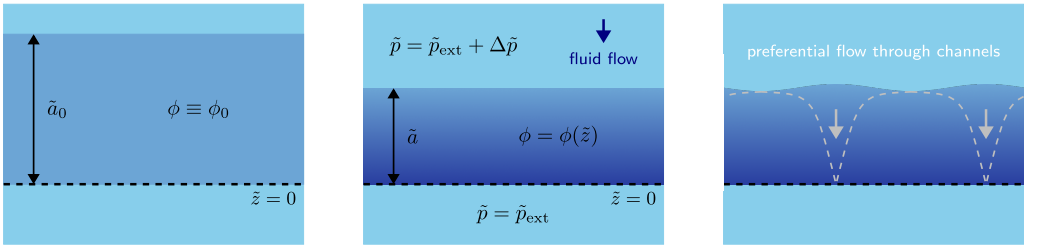


Figure 2: On the left, the undeformed base state where the fluid pressure is the same both above and below the fully-swollen gel and there is no compression, so the uniform hydrogel layer occupies the region $0 \leqslant \tilde{z} \leqslant \tilde{a}_0$. In the centre, the steady state when a pressure difference $\Delta\tilde{p}$ is applied across the layer is pictured, with a polymer fraction that increases with depth and a corresponding compaction of the thickness to $\tilde{a} < \tilde{a}_0$. On the right, the formation of channels in this steady state is illustrated schematically, wherein water flows preferentially through certain regions of the gel.

2. Pressure-driven deformation of gel layers

In order to understand the static compaction profile for poroelastic media, we consider a layer of hydrogel (or equivalently any other cross-linked poroelastic material) occupying the region $0 \leqslant \tilde{z} \leqslant \tilde{a}$ and with infinite extent in the horizontal ($\tilde{x}$ and $\tilde{y}$) directions parallel to its base. The upper free surface is exposed to water at fixed pressure $\tilde{p} = \tilde{p}_{\text{ext}} + \Delta\tilde{p}$, whilst the lower surface is held at $\tilde{z} = 0$ by a fixed, solid membrane which is perfectly permeable to water, at pressure $\tilde{p} = \tilde{p}_{\text{ext}}$. Thus, a fluid flow is driven vertically downwards, through the porous hydrogel and into the pure fluid layer below. This physical setup is illustrated in figure 2. In the present study, we neglect the effect of gravity on the dynamics of the problem, and consider instead force-free equilibrium to derive our equations of motion, as is standard when considering the slow flows in, for example, hydrogels (MacMinn *et al.* 2016), though of course gravity could be the source of the pressure difference across the layer.

2.1. *Governing equations of poroelasticity*

The theory of poroelasticity is built by combining flow through and deformation of porous media, with the coupling between these two processes provided by stresses exerted by and on the solid scaffold. For our purposes, and indeed many poroelastic problems, the viscous stress exerted on the elastic scaffold by the fluid flow can be neglected for the solid-mechanical problem, and the coupling becomes one-way, with elastic stresses from the matrix setting fluid pressures and thus driving interstitial flows (Coussy 2004). This is a result of strain rates having a significantly smaller effect on stress (through the viscous part of the fluid stress tensor) than strain does in the elastic solid stress tensor. Viscous stresses associated with fluid flows are not entirely neglected in the fluid dynamics, however – viscosity sets the flow rates as a function of pressure drop by Darcy's law,

$$\tilde{\boldsymbol{u}} = -\frac{1}{\mu_l}\tilde{\boldsymbol{k}} \cdot \tilde{\boldsymbol{\nabla}}\tilde{p}, \tag{2.1}$$

where μ_l is the dynamic viscosity of the fluid, $\tilde{\boldsymbol{k}}$ is the permeability tensor, $\tilde{p}$ is the pore (or pervadic, or Darcy – a full discussion is provided in Peppin *et al.* (2005)) pressure and $\tilde{\boldsymbol{u}}$ is a fluid flux per unit area measured relative to a stationary porous medium. If the solid volume fraction of a porous medium is ϕ (and thus its porosity is $1 - \phi$), $\tilde{\boldsymbol{u}}$ can be expressed in terms of the solid and fluid velocities $\tilde{\boldsymbol{u}}_{\boldsymbol{s}}$ and $\tilde{\boldsymbol{u}}_{\boldsymbol{f}}$ by $\tilde{\boldsymbol{u}} = (1 - \phi)(\tilde{\boldsymbol{u}}_{\boldsymbol{f}} - \tilde{\boldsymbol{u}}_{\boldsymbol{s}})$. As such, at a fixed

Focus on Fluids articles must not exceed this page length

boundary such as that found at $\tilde{z} = 0$, $\tilde{\boldsymbol{u}}$ quantifies the fluid flow into or out of the poroelastic material.

In order to close the flow problem, we must now quantify the coupling between gradients in $\tilde{p}$ and deformation of the matrix. Following Terzaghi (1925) and Biot (1941), the Cauchy stress on a volume element can be written as

$$\tilde{\sigma} = -\tilde{p}\boldsymbol{I} + \tilde{\sigma}^{(\boldsymbol{e})}, \tag{2.2}$$

where $\tilde{\sigma}^{(\boldsymbol{e})}$ is the effective stress tensor, a function of the displacement of the scaffold elements from their equilibrium positions, and the only stress we consider from the fluid phase is its pressure p. Conservation of momentum in the force-free case implies that

$$\tilde{\boldsymbol{\nabla}} \cdot \tilde{\sigma} = \boldsymbol{0} \quad \text{so} \quad \tilde{\boldsymbol{u}} = -\frac{1}{\mu_l}\tilde{\boldsymbol{k}} \cdot \tilde{\boldsymbol{\nabla}} \cdot \tilde{\sigma}^{(\boldsymbol{e})}. \tag{2.3}$$

In this work, we will only consider poroelastic media with isotropic permeability that may depend on the porosity, so $\tilde{\boldsymbol{k}} = \tilde{k}(\phi)\boldsymbol{I}$. This relation allows us to model the dynamics solely in terms of the configuration of the solid matrix.

For the effective stress, we use the linear-elastic-nonlinear-swelling model for hydrogels (Webber & Worster 2023), measuring all deformations from a reference 'fully-swollen' state $\phi \equiv \phi_0$. This is the state that the medium would reach everywhere in the absence of external stress when placed in water. Deformations from this swollen state are described by a displacement vector field $\boldsymbol{\xi}$ from which we can define the Cauchy strain tensor

$$\boldsymbol{e} = \text{sym}\,(\boldsymbol{\nabla}\boldsymbol{\xi}) = \left[1 - \left(\frac{\phi}{\phi_0}\right)^{1/3}\right]\boldsymbol{I} + \epsilon, \tag{2.4}$$

where ϵ is the deviatoric part of the tensor and the isotropic part corresponds to volumetric changes. On the assumption of leading-order isotropic deformation, the effective stress tensor is

$$\tilde{\sigma}^{(\boldsymbol{e})} = -\tilde{\Pi}(\phi)\boldsymbol{I} + 2\tilde{\mu}_s(\phi)\epsilon, \tag{2.5}$$

where $\tilde{\Pi}$, the generalised osmotic pressure, characterises isotropic matrix stresses and $\tilde{\mu}_s$, the shear modulus, relates deviatoric strains to stresses. Assuming that the deviatoric strain is small (i.e. all components of ϵ are below the threshold of ~ 0.1 where linear elasticity can be reasonably assumed to apply), one can derive an expression for $\tilde{\boldsymbol{\nabla}} \cdot \tilde{\sigma}^{(\boldsymbol{e})}$ in terms of the generalised osmotic pressure $\tilde{\Pi}(\phi)$ and the shear modulus $\tilde{\mu}_s(\phi)$ (Webber & Worster 2023), implying that

$$\tilde{\boldsymbol{u}} = \frac{\tilde{k}(\phi)}{\mu_l}\left[\frac{\partial\tilde{\Pi}}{\partial\phi} + \frac{4\tilde{\mu}_s(\phi)}{3\phi}\left(\frac{\phi}{\phi_0}\right)^{1/3}\right]\tilde{\boldsymbol{\nabla}}\phi. \tag{2.6}$$

In effect, this shows that interstitial flows are driven from swollen to dried areas, along gradients in ϕ, with a poroelastic diffusivity linking the gradients in ϕ to fluxes. The assumption of small deviatoric strains will be relaxed in the following analysis, with the model detailed above providing a clear physical separation between isotropic and deviatoric components of stress and their different effects on the fluid mechanics of the problem, providing insight into the qualitative processes driving instability. It could then be exchanged for a number of different fully nonlinear approaches if strong agreement with experimental data was required.

2.2. *Equations for steady state*

In order to seek a steady state profile, we use the equations of solid and water conservation,

$$\frac{\partial \phi}{\partial \tilde{t}} + \tilde{\boldsymbol{\nabla}} \cdot (\phi \tilde{\boldsymbol{u}}_{\boldsymbol{s}}) = 0 \quad \text{and} \quad \frac{\partial}{\partial \tilde{t}}(1-\phi) + \tilde{\boldsymbol{\nabla}} \cdot \left[(1-\phi)\tilde{\boldsymbol{u}}_{\boldsymbol{f}}\right] = 0. \tag{2.7}$$

where $\tilde{\boldsymbol{u}}_{\boldsymbol{s}}$ and $\tilde{\boldsymbol{u}}_{\boldsymbol{f}}$ are the solid and fluid velocities, respectively. These can be combined to give

$$\frac{\partial \phi}{\partial \tilde{t}} + \left[\phi \tilde{\boldsymbol{u}}_{\boldsymbol{s}} + (1-\phi)\tilde{\boldsymbol{u}}_{\boldsymbol{f}}\right] \cdot \tilde{\boldsymbol{\nabla}} \phi = \tilde{\boldsymbol{\nabla}} \cdot (\phi \tilde{\boldsymbol{u}}) \tag{2.8}$$

In steady state, $\tilde{\boldsymbol{u}}_{\boldsymbol{s}}$ must be zero, and therefore this equation implies that $\tilde{\boldsymbol{\nabla}} \cdot \tilde{\boldsymbol{u}} = 0$, which can be further simplified to $\partial(\tilde{\boldsymbol{u}} \cdot \hat{\boldsymbol{z}})/\partial \tilde{z} = 0$ on the assumption that all flows and heterogeneities are in the vertical direction. This is to be expected; in a steady state, the fluid flow must be uniform or else swelling or drying would be needed to enforce conservation of mass.

Non-dimensionalising and assuming that the shear modulus is a constant independent of ϕ (a reasonable assumption in many gel models, justified in the appendix of Webber & Montenegro-Johnson (2025)), let

$$\Phi = \frac{\phi}{\phi_0};\ k = \frac{\tilde{k}(\phi)}{k_0};\ \Pi = \frac{\tilde{\Pi}(\phi)}{\Pi_0};\ p = \frac{\tilde{p}}{\Pi_0};\ \mathcal{M} = \frac{\mu_s}{\Pi_0};\ \mathcal{P} = \frac{\Delta \tilde{p}}{\Pi_0};\ z = \frac{\tilde{z}}{a_0};\ a = \frac{\tilde{a}}{a_0}, \tag{2.9}$$

where k_0 and Π_0 are representative scales for the permeability and osmotic pressure, respectively. Then, the steady-state profile must satisfy

$$\frac{\partial}{\partial z}\left\{k(\Phi)\left[\frac{\partial \Pi}{\partial \Phi} + \frac{4\mathcal{M}}{3}\Phi^{-2/3}\right]\frac{\partial \Phi}{\partial z}\right\} = 0. \tag{2.10a}$$

Conservation of polymer sets the value of the scaled poroelastic layer thickness $a = \tilde{a}/a_0$ implicitly through

$$\int_0^a \Phi \, \mathrm{d}z = 1. \tag{2.10b}$$

2.3. *Boundary conditions and steady states*

At both the upper and lower surfaces of the gel layer, $z = 0$, a, there is continuity of fluid pressure, and so $p = p_{\text{ext}} + \mathcal{P}$ on $z = a$ and $p = p_{\text{ext}}$ on $z = 0$. There is not, however, continuity of normal stress on the lower boundary, since the porous mesh supports the gel and holds it at $z = 0$ by applying an upward force. At $z = a$, continuity of stress at the uppermost boundary implies that the effective stress must be zero, and so, taking the normal component,

$$\Pi(\Phi) - 2\mathcal{M}\epsilon_{zz} = 0 \quad \text{with} \quad \epsilon_{zz} = \frac{\partial \eta}{\partial z} - 1 + \Phi^{1/3}, \tag{2.11}$$

where η is the (scaled) vertical displacement of the topmost surface from its equilibrium position $z = 1$. On the assumption that all compression occurs in the vertical direction (i.e. plane strain), with no displacements parallel to the base of the gel, this vertical displacement can be deduced from polymer conservation. Hence,

$$\frac{\partial \eta}{\partial z} = 3\left(1 - \Phi^{1/3}\right) \quad \text{so that} \quad \Pi(\Phi) = 4\mathcal{M}\left(1 - \Phi^{1/3}\right) \text{ on } z = a, \tag{2.12}$$

giving an implicit expression solely in terms of Φ which can be solved for the polymer fraction at $z = a$ (Webber & Worster 2023). The only permissible solution to this relation

is $\Phi = 1$, since $\Pi > 0$ for $\Phi > 1$ yet the right-hand side is negative in such cases (and similar arguments prevent $\Phi < 1$). The system is closed by a condition linking the gradients in pressure through the gel to the pressure from the fluid above the gel, using equation (2.6) and Darcy's law to find

$$\frac{\partial p}{\partial z} = -\left(\frac{\partial \Pi}{\partial \Phi} + \frac{4\mathcal{M}}{3}\Phi^{-2/3}\right)\frac{\partial \Phi}{\partial z} = -\frac{\partial}{\partial z}\left(\Pi(\Phi) + 4\mathcal{M}\Phi^{1/3}\right), \tag{2.13}$$

and so, integrating from $z = 0$ to $z = a$,

$$\Delta\tilde{p}/\Pi_0 = \mathcal{P} = \left[\Pi(\Phi) + 4\mathcal{M}\Phi^{1/3}\right]_a^0 = \Pi\big(\Phi|_{z=0}\big) + 4\mathcal{M}\left(\Phi|_{z=0}^{1/3} - 1\right). \tag{2.14}$$

This condition sets the basal solid fraction in terms of the overpressure, with a drier base if the scaled driving pressure $\mathcal{P}$ is higher. Therefore, to find a steady state solution, we solve equation (2.10*a*) alongside boundary conditions $\Phi = 1$ on $z = a$ and (2.14) on $z = 0$, with the thickness a set by equation (2.10*b*).

2.4. *Forms of $k(\Phi)$ and $\Pi(\Phi)$*

In order to solve this system, we require a functional form for both the permeability in terms of solid fraction and the generalised osmotic pressure. In general, the permeability is a decreasing function of polymer fraction, since we expect increasing porosity to lead to less viscous resistance. The commonly-used Kozeny-Carman relation gives

$$k \propto \frac{(1-\phi)^3}{\phi^2}, \tag{2.15}$$

which reduces to $k \propto \phi^{-2}$ in the limit $\phi \ll 1$, which holds well in the case of a dense packing of spheres. Etzold *et al.* (2021) instead use a form $k \propto \phi^{-2/3}$ for beads of polyacrylamide hydrogel, and recent experiments by Feng *et al.* (2026) suggest an even stronger dependence $k \propto \phi^{-4.6}$ in poly(ethylene glycol) diacrylate (PEGDA) gels. In this study, we will allow for any of these cases by prescribing $k(\Phi) = \Phi^{-\alpha}$ for $\alpha \geqslant 0$. Unlike the generalised form taken in Hewitt *et al.* (2016), this permeability never reaches zero, and so fluxes will not be permitted to reach zero when there is a nonzero hydrostatic head.

The generalised osmotic pressure can either be deduced from a thermodynamic foundation, with contributions from entropic mixing of solid and fluid phases , elasticity of the matrix and any hydrophilic contributions (Webber & Montenegro-Johnson 2025), or can be fitted phenomenologically to experimental data, such as that of Feng *et al.* (2025). Experiments suggest that the former approach, which gives logarithmic dependence of Π on Φ at leading order, is inaccurate (Feng *et al.* 2026), and so we choose the latter approach here and take

$$\Pi(\Phi) = \frac{\Phi - 1}{1 - \Phi/\Phi_C}, \tag{2.16}$$

which satisfies the two key properties required of a generalised osmotic pressure; firstly, that it is equal to zero at $\Phi = 1$, and secondly that it asymptotes at a finite 'maximally-dry' polymer fraction $\Phi_C > 1$. Close to equilibrium swelling, or when $\Phi \ll \Phi_C$, Π is also approximately linear in this case, which gives analytic tractability, but it is also shown in Webber & Worster (2025) that this functional form fits experimental measurements well.

2.5. *Compression profiles*

There are some special cases where the base state can be solved for analytically; specifically cases of super-absorbent poroelastic media ($\Phi_C \gg 1$) with zero shear modulus and $\alpha = 1$.

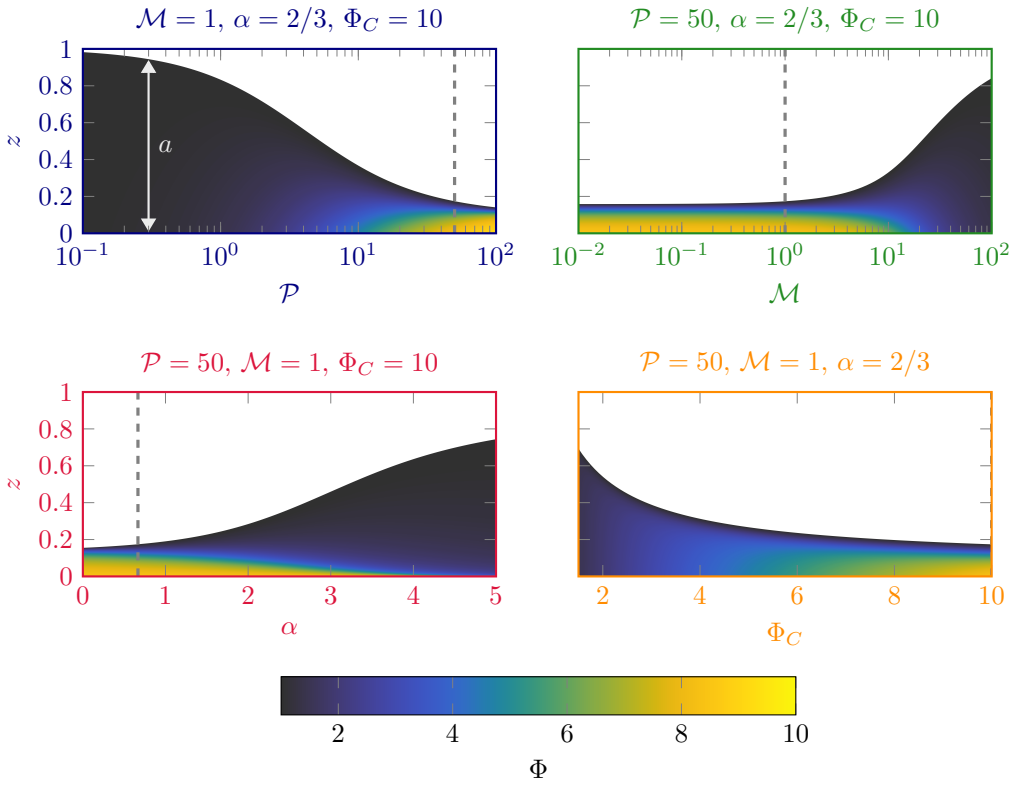


Figure 3: Plots of the polymer fraction profile against depth for different driving pressures $\mathcal{P}$, stiffness parameters $\mathcal{M}$, permeability exponents α and maximum solid fractions Φ_C.

In this case, equation (2.10*a*) has solution

$$\Phi = (1 + \mathcal{P})e^{-\mathcal{P}z} \quad \text{with} \quad a = \frac{\ln(1 + \mathcal{P})}{\mathcal{P}}. \tag{2.17}$$

These analytic results make it very clear how the thickness of the gel decreases at a decreasing rate with increasing pressure $\mathcal{P}$, and how the (scaled) polymer fraction decays exponentially from $1 + \mathcal{P}$ to 1 on its base towards the top.

More generally, the system of equations (2.10) can be solved numerically for different parameter values to find the steady-state solid fraction profiles and compressions, as plotted in figure 3. Appendices A and B solve for the compressions analytically in the large- and small-$\mathcal{M}$ limits, respectively.

In general, increasing the pressure difference (the value of $\mathcal{P}$) leads to a greater compression of the poroelastic medium, which remains fully-swollen on its uppermost surface but has an increasing polymer fraction as depth increases, as would be expected. This is shown in the first panel of figure 3, where the thickness a decreases and plateaus at $1/\Phi_C$ as $\mathcal{P} \to \infty$. A larger contribution from shear, however, leads to both a smaller amount of compression (setting a lower basal value of Φ) and much less significant gradients in Φ with depth. This again is to be expected, since stiff gels resist anisotropy in deswelling, preferring to reach as uniform a deswelling profile as possible.

Less immediately obvious is the effect of changing Φ_C and α. When α is larger, dewatering the gel leads to a more significant reduction in hydraulic conductivity and therefore the amount of compression that it is possible to produce reduces for a given stiffness and hydraulic head.

In a sense, a higher value of α creates a hydraulic bottleneck on the base of the gel, shielding the rest of the layer from a need to compress. If Φ_C is larger, the capacity of the gel to deswell under compression is significantly greater, and therefore there is more drying and more compression.

2.5.1. *Flux magnitudes and stiffness*

Increasing the pressure head $\mathcal{P}$ will lead to higher fluxes since the flow magnitude depends on pressure gradients. Not only does a larger pressure differential either side of the gel layer provide such an effect, but also greater compression of the gel layer reduces the distance over which this pressure drops. Working in the other direction to both of these effects is the fact that the permeability also reduces with greater compression, therefore reducing the magnitude of fluxes. In other studies, the specific choice of stress and permeability constitutive relations allow for a flux that reaches a constant plateau when these competing effects balance (Hewitt *et al.* 2016) or for a flux that drops to zero if the poroelastic material is allowed to compact to zero porosity (Ghosh *et al.* 2026), a process referred to as 'pore closure'.

In our model, the relationship between the magnitude of the dimensionless flux

$$Q = \Phi^{-\alpha}\left[\frac{1-1/\Phi_C}{(1-\Phi/\Phi_C)^2} + \frac{4\mathcal{M}}{3}\Phi^{-2/3}\right]\frac{\partial \Phi}{\partial z} \tag{2.18}$$

and the applied pressure head is always monotonic, but at large values of $\mathcal{P}$ the relationship approaches a linear one, since the polymer fraction becomes close to Φ_C everywhere, with $a \to 1/\Phi_C$. Hence the permeability and layer thickness approach constants, and Darcy's law reduces to a statement of direct proportionality.

In figure 4, it is illustrated that, for sufficiently low values of $\mathcal{P}$, the pressure–flux relationship is nonlinear, as stresses are balanced by an anisotropic elastic response. However, for larger $\mathcal{P}$, there is no further meaningful compaction (the bulk of the gel layer is close to $\Phi = \Phi_C$) and so the pressure head–flux relationship is approximately linear, as would be expected from Darcy's law. Increasing the stiffness parameter $\mathcal{M}$ leads to a smaller flux for a fixed value of $\mathcal{P}$ since the thickness of the compacted matrix is greater when the gel is stiffer. The second panel of figure 4 shows the depth-averaged permeability $\bar{k}$, defined by

$$\bar{k} = \frac{1}{a}\int_0^a \Phi^{-\alpha}\,\mathrm{d}z, \tag{2.19}$$

showing a plateau towards ever-higher values as $\mathcal{M}$ is increased. For large $\mathcal{P}$, this illustrates how the poroelastic bed simply acts as a uniform porous bed of effective permeability $\bar{k}$, explaining the linear relationship between u and $\mathcal{P}$ in this case.

At a fixed value of $\mathcal{P}$, however, the effect of changing the stiffness on the fluid flux carried through the gel layer is not straightforward. Rearranging Darcy's law, we find

$$Q = -\frac{\mathcal{P}}{\int_0^a \Phi^{\alpha}\,\mathrm{d}z}, \tag{2.20}$$

which, dependent on the value of α, may give a flux magnitude that increases or decreases with $\mathcal{M}$, owing to the competing effects of increased permeability and increased distance over which to transport as stiffness increases and the extent of compaction becomes less. In the large-$\mathcal{M}$ limit, appendix A shows that fluxes increase with $\mathcal{M}$ only when $\alpha > 1$. Otherwise, increasing the stiffness decreases the magnitude of fluxes.

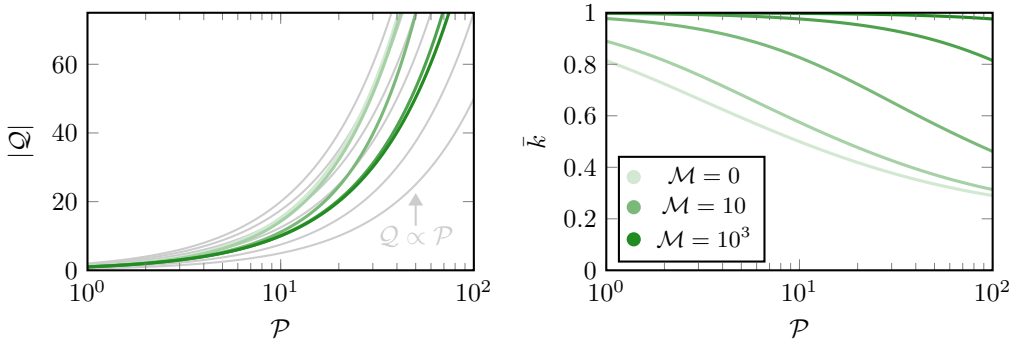


Figure 4: Plots of the fluid flux magnitudes against pressure head $\mathcal{P}$ and the depth-averaged permeability $\bar{k}$, both with $\alpha = 2/3$, as the stiffness parameter $\mathcal{M}$ is varied. On the left, notice that stiffer gels have a more linear pressure-velocity relation (some representative examples of this are plotted in grey), explained by the right-hand plot showing that $\bar{k}$ (and, indeed, a) has little dependence on $\mathcal{P}$ when the gel is stiff.

3. Stability of compressed profiles

In a hydrogel with a significant shear modulus, there is a strong preference for any deformation from fully-swollen equilibrium to be isotropic in nature, since any deviatoric strains lead to deviatoric stresses. Indeed, this preference is exploited in the LENS model to linearise around small deviatoric deformation. The steady flow-driven compaction states outlined above have all deformation constrained to be in the vertical direction, and so any significant compaction can generate large deviatoric stresses, which it would be energetically favourable to relieve. As is seen in studies of hydrogel wrinkling (Webber & Worster 2024), one possible way in which such stresses are relieved is by preferentially swelling 'channels' which can act as low-permeability conduits carrying fluid through a gel, relieving deviatoric stress by swelling certain regions closer to an isotropic state. This instability is entirely elastic in nature and we will show that the compacted porous layers are instead unstable to a flow-driven instability which qualitatively looks similar, even though it grows by a different mechanism.

To probe the stability of such a state, we assume that the initial (base state) deformation from the fully-swollen reference state is described by the displacement vector field $\boldsymbol{\xi_0}(\boldsymbol{x}) = \eta_0(z)\hat{\boldsymbol{z}}$, where

$$\boldsymbol{\nabla} \cdot \boldsymbol{\xi_0} = 3\left(1 - \Phi_0^{1/3}\right), \tag{3.1}$$

with $\Phi_0 = \phi/\phi_0$ the steady-state profile deduced in the previous section. As before, we scale all lengths with a_0. Now, perturb the displacement vector field with a wavelike disturbance with components perpendicular and parallel to the base of the gel and wavevector $\boldsymbol{k} = (k_x,\, k_y,\, 0)^{\mathrm{T}}$,

$$\boldsymbol{\xi} = \boldsymbol{\xi_0} + \epsilon\boldsymbol{\xi_1} = \eta_0(z)\hat{\boldsymbol{z}} + \varepsilon\left[\boldsymbol{\xi}_{\parallel}(z) + \eta_1(z)\hat{\boldsymbol{z}}\right] e^{\mathrm{i}\boldsymbol{k}\cdot\boldsymbol{x}+st}, \tag{3.2}$$

where $\varepsilon \ll 1$ is some small instability amplitude and $\boldsymbol{\xi}_{\parallel}$ is the component of the displacement parallel to the base (i.e. $\boldsymbol{\xi}_{\parallel}\cdot\hat{\boldsymbol{z}} = 0$). s is the (scaled) growth rate of this perturbation, after time has been non-dimensionalised with the poroelastic timescale $\mu_l a_0^2/k_0\Pi_0$ (see, for example, Godard *et al.* (2025)).

Since the base state is dependent only on z, we can choose a coordinate system aligned with the wavevector such that $\boldsymbol{k} = \gamma\hat{\boldsymbol{x}}$ without any loss of generality, defining $\xi_{\parallel} = \boldsymbol{\xi}_{\parallel}\cdot\hat{\boldsymbol{x}}$. This reduces the problem to a two-dimensional one, whilst still incorporating three-dimensional volumetric effects. Given this perturbation to the displacement field, we can use the same expression relating the divergence of the displacement field to the polymer fraction (2.4) to

Rapids articles must not exceed this page length

deduce the perturbation to the local polymer fraction,

$$\Phi = \Phi_0(z) + \varepsilon\Phi_1(z)e^{\mathrm{i}\gamma x+st} \quad \text{where} \quad \mathrm{i}\gamma\xi_\parallel(z) + \eta_1'(z) = -\Phi_0^{-2/3}\Phi_1 = -\Psi(z). \tag{3.3}$$

Here, the function $\Psi(z)$ has been introduced for convenience. It represents the perturbation to $\boldsymbol{\nabla}\cdot\boldsymbol{\xi}$ and therefore measures the linear compression introduced by the perturbation displacement. To deduce the growth or shrinkage of such a perturbation, we need to firstly consider the elastic problem and the associated perturbations to pore pressure before then using the equation for gel swelling to deduce whether these perturbations can increase in magnitude.

3.1. *The elastic problem*

The order-ε perturbations to the displacement vector field and polymer fraction field lead to similar perturbations to the total stress tensor $\boldsymbol{\sigma} = \boldsymbol{\sigma_0} + \varepsilon\boldsymbol{\sigma_1}e^{\mathrm{i}\gamma x+st}$ and the total pressure field $P = p + \Pi$, all non-dimensionalised by Π_0 as before, such that

$$\boldsymbol{\sigma_1} = -P_1\mathbf{I} + \mathcal{M}\left[\boldsymbol{\nabla\xi_1} + (\boldsymbol{\nabla\xi_1})^{\mathrm{T}} + \frac{2}{3}\Psi(z)\mathbf{I}\right], \tag{3.4}$$

where $P = P_0 + \epsilon P_1$ and the deviatoric strain is written in terms of $\boldsymbol{\xi}$ using equation (2.4). Noting that $\boldsymbol{\nabla}\cdot\boldsymbol{\xi_1} = -\Psi(z)$, we take the divergence of this tensor to find

$$\boldsymbol{\nabla}\left[P_1 + \frac{\mathcal{M}}{3}\Psi(z)\right] = \mathcal{M}\nabla^2\boldsymbol{\xi_1}. \tag{3.5}$$

Consider first the $\hat{\boldsymbol{z}}$ component of this equation,

$$\frac{\partial}{\partial z}\left[P_1 + \frac{\mathcal{M}}{3}\Psi(z)\right] = \mathcal{M}\left[\eta_1''(z) - \gamma^2\eta_1(z)\right], \tag{3.6}$$

where $'$ denotes a derivative with respect to z. The horizontal component of equation (3.5) is

$$\mathrm{i}\gamma\left[P_1 + \frac{\mathcal{M}}{3}\Psi(z)\right] = \mathcal{M}\left[\xi_\parallel''(z) - \gamma^2\xi_\parallel(z)\right], \tag{3.7}$$

Now, recalling from equation (3.3) that

$$\mathrm{i}\gamma\xi_\parallel = -\left[\Psi(z) + \eta_1'(z)\right], \tag{3.8}$$

multiply both sides of the horizontal momentum balance (3.7) by $\mathrm{i}\gamma$ to find

$$\gamma^2\left[P_1 + \frac{\mathcal{M}}{3}\Psi(z)\right] = \mathcal{M}\left[\Psi(z) + \eta_1'(z)\right]'' - \mathcal{M}\gamma^2\left[\Psi(z) + \eta_1'(z)\right]. \tag{3.9}$$

Differentiating the vertical balance (3.6) with respect to z gives

$$\left[P_1 + \frac{\mathcal{M}}{3}\Psi(z)\right]'' = \mathcal{M}\left[\eta_1'''(z) - \gamma^2\eta_1'(z)\right]. \tag{3.10}$$

Subtract equation (3.9) from (3.10) to find

$$\mathcal{L}\left[P_1 + \frac{\mathcal{M}}{3}\Psi(z)\right] = -\mathcal{M}\mathcal{L}[\Psi(z)] \quad \text{with} \quad \mathcal{L} = \frac{\partial^2}{\partial z^2} - \gamma^2. \tag{3.11}$$

Now, introduce the quantity $Z(z) = P_1(z) + (4\mathcal{M}/3)\Psi(z)$, allowing us to deduce

$$\mathcal{L}[Z] = 0 \quad \text{and} \quad \mathcal{M}\mathcal{L}[\eta_1] = Z' - \mathcal{M}\Psi'. \tag{3.12}$$

3.2. *The swelling problem*

The dynamics governing growth or decay of the instability are governed by the swelling equation (2.8), which depends on the perturbation fluid flux. The dimensionless fluid flux is given in terms of gradients in the scaled pore pressure $p = p_0 + \varepsilon p_1 e^{\mathrm{i}\gamma x + st}$ by

$$\boldsymbol{u} = -k(\Phi)\boldsymbol{\nabla} p = -k(\Phi_0)\boldsymbol{\nabla} p_0 - \varepsilon\left[k'(\Phi_0)\Phi_1\boldsymbol{\nabla} p_0 + k(\Phi_0)\boldsymbol{\nabla} p_1\right] e^{\mathrm{i}\gamma x + st}. \tag{3.13}$$

Thus, assuming that $k = \Phi^{-\alpha}$, the perturbation fluid flux (hereafter dropping factors of $e^{\mathrm{i}\gamma x + st}$) is

$$\boldsymbol{u_1} = -\left[\Phi_0^{-\alpha}\boldsymbol{\nabla} p_1 - \alpha\Phi_0^{-(\alpha+1)}\Phi_1\frac{\partial p_0}{\partial z}\hat{\boldsymbol{z}}\right], \tag{3.14}$$

where $\Phi_0^{-\alpha}\,\partial p_0/\partial z = -Q$ is a constant equal to the depth-independent downwards flux in the base state. Hence,

$$\boldsymbol{\nabla}\cdot\boldsymbol{u_1} = -\boldsymbol{\nabla}\cdot\left(\Phi_0^{-\alpha}\boldsymbol{\nabla} p_1\right) - \alpha Q\frac{\partial}{\partial z}\left(\Phi_0^{-1}\Phi_1\right). \tag{3.15}$$

Then, replacing Φ_1 with $\Phi_0^{2/3}\Psi(z)$ and computing the gradients,

$$\Phi_0\boldsymbol{\nabla}\cdot\boldsymbol{u_1} = \alpha\Phi_0^{-\alpha}\Phi_0' p_1' - \Phi_0^{-(\alpha-1)}\mathcal{L}[p_1] - \alpha Q\Phi_0\frac{\partial}{\partial z}\left(\Phi_0^{-1/3}\Psi\right), \tag{3.16}$$

and equation (2.8) shows that this must be equal to $\partial\Phi_1/\partial t + (\boldsymbol{u_s}\cdot\hat{\boldsymbol{z}})\,\partial\Phi_0/\partial z$, given by

$$s\left(\Phi_1 + \Phi_0^{-1/3}\eta_1\Phi_0'\right) = s\Phi_0^{2/3}\left(\Psi + \Phi_0^{-1}\Phi_0'\eta_1\right), \tag{3.17}$$

using the fact that $\boldsymbol{u_s} = \Phi^{-1/3}\,\partial\xi/\partial t$ at leading order (Webber *et al.* 2023). Hence,

$$\Phi_0^{-\alpha}\Phi_0' p_1' - \Phi_0^{-(\alpha-1)}\mathcal{L}[p_1] - Q\alpha\Phi_0\frac{\partial}{\partial z}\left(\Phi_0^{-1/3}\Psi\right) = s\Phi_0^{2/3}\left(\Psi + \Phi_0^{-1}\Phi_0'\eta_1\right). \tag{3.18}$$

Finally, note

$$p_1 = Z - \frac{4\mathcal{M}}{3}\Psi - \left.\frac{\mathrm{d}\Pi}{\mathrm{d}\Phi}\right|_{\Phi_0}\Phi_1 = Z - \left[\frac{4\mathcal{M}}{3} + \left.\frac{\mathrm{d}\Pi}{\mathrm{d}\Phi}\right|_{\Phi_0}\Phi_0^{2/3}\right]\Psi, \tag{3.19}$$

so equation (3.18) can be rewritten, using the result for $\mathcal{L}[Z]$ from equation (3.12), as

$$\begin{aligned}\mathcal{L}\left[\left(\frac{4\mathcal{M}}{3} + \left.\frac{\mathrm{d}\Pi}{\mathrm{d}\Phi}\right|_{\Phi_0}\Phi_0^{2/3}\right)\Psi\right] &= s\Phi_0^{\alpha-1/3}\left(\Psi + \Phi_0^{-1}\Phi_0'\eta_1\right) + Q\alpha\Phi_0^{\alpha}\frac{\partial}{\partial z}\left(\Phi_0^{-1/3}\Psi\right)\\ &\quad - \Phi_0^{-1}\Phi_0'\frac{\partial}{\partial z}\left[\left(\frac{4\mathcal{M}}{3} + \left.\frac{\mathrm{d}\Pi}{\mathrm{d}\Phi}\right|_{\Phi_0}\Phi_0^{2/3}\right)\Psi\right].\end{aligned} \tag{3.20}$$

Solving this swelling equation is somewhat challenging. It involves derivatives of the poroelastic 'conductivity' multiplied by the swelling extent. In order to demonstrate the processes driving the instability without perhaps capturing the nuance of functional form of $\Pi(\Phi)$ introduced above, we assume that Π is a linear function of Φ and equal to $\Phi - 1$, in effect the $\Phi_C \gg 1$ limit of equation (2.16).

3.3. *Boundary conditions*

The model described by equations (3.12) and (3.20) is a sixth-order system with an unknown growth rate s, and therefore we require seven conditions to close the problem. Perhaps the

simplest of these are on the displacement, which must be zero on the base. Thus,

$$\eta_1(0) = 0 \quad \text{and} \quad \Psi(0) + \eta_1'(0) = 0. \tag{3.21}$$

using (3.8) for the horizontal displacement.

Pore pressure must be continuous across both boundaries, by definition. This is simplest to impose on $z = 0$, where $p_1 = 0$ and so

$$Z(0) = \left[\frac{4\mathcal{M}}{3} + \left.\frac{\mathrm{d}\Pi}{\mathrm{d}\Phi}\right|_{\Phi_0(0)} \Phi_0(0)^{2/3}\right]\Psi(0). \tag{3.22}$$

On the uppermost boundary, we must incorporate the effect of deforming the gel itself. Hence, since the top boundary is at $z = a + \varepsilon\eta_1$, $p_1(a) + \eta_1\, \partial p_0/\partial z\,|_{z=a} = 0$ and

$$Z(a) - \left[\frac{4\mathcal{M}}{3} + \left.\frac{\mathrm{d}\Pi}{\mathrm{d}\Phi}\right|_1\right]\Psi(a) = \mathcal{Q}\eta_1(a), \tag{3.23}$$

using the fact that the permeability is scaled to unity on $z = a$.

We use the expression of (3.4) to deduce stress boundary conditions on the top surface, first enforcing zero normal stress

$$-P_1(a) + 2\mathcal{M}\eta_1'(a) + \frac{2\mathcal{M}}{3}\Psi(a) = 0 \quad \text{so} \quad Z(a) = 2\mathcal{M}\left[\eta_1'(a) + \Psi(a)\right]. \tag{3.24}$$

Finally, there is no shear stress on the wavy surface of the gel in contact with water. Thus,

$$\mathrm{i}\gamma\eta_1 + \xi_\parallel'(a) = 0, \tag{3.25}$$

which, alongside equations (3.8) and (3.12), implies

$$Z'(a) + 2\mathcal{M}\gamma^2\eta_1(a) = 0. \tag{3.26}$$

A seventh condition can be found by choosing a normalisation for the perturbation eigenfunctions, since the entire problem here can be scaled by some multiplicative factor, owing to linearity. For the sake of preventing any of the perturbation quantities 'blowing up', we assume

$$1 = \int_0^a |Z|^2 + |\Psi|^2 + |\eta_1|^2 + \left|\xi_\parallel\right|^2 \,\mathrm{d}z, \tag{3.27}$$

where $\left|\xi_\parallel\right|^2 = \left|\Psi + \eta_1'\right|^2/\gamma^2$, again using equation (3.3).

4. Investigating the stability of compacted media

Making the linear osmotic pressure assumption above, so $\partial\Pi/\partial\Phi = 1$, our governing equations are

$$\mathcal{L}[Z(z)] = 0, \tag{4.1a}$$

$$\mathcal{L}[\eta_1(z)] = \frac{1}{\mathcal{M}}Z'(z) - \Psi'(z), \tag{4.1b}$$

$$\left(\frac{4\mathcal{M}}{3} + \Phi_0^{\frac{2}{3}}\right)\mathcal{L}[\Psi(z)] = \left[s\Phi_0^{\alpha-\frac{1}{3}} - \frac{1}{3}\alpha\mathcal{Q}\Phi_0^{\alpha-\frac{4}{3}}\Phi_0' - \frac{4}{9}\Phi_0^{-\frac{4}{3}}\Phi_0'^2 - \frac{2}{3}\Phi_0^{-\frac{1}{3}}\Phi_0''\right]\Psi(z) +$$
$$\left[\alpha\mathcal{Q}\Phi_0^{\alpha-\frac{1}{3}} - \frac{4\mathcal{M}}{3}\Phi_0^{-1}\Phi_0' - \frac{7}{3}\Phi_0^{-\frac{1}{3}}\Phi_0'\right]\Psi'(z) + s\Phi_0^{\alpha-\frac{4}{3}}\Phi_0'\eta_1(z). \tag{4.1c}$$

The boundary and normalisation conditions in this case become

$$\eta_1(0) = 0, \quad \Psi(0) + \eta_1'(0) = 0 \quad \text{and} \quad Z(0) = \left[\Phi_0(0)^{2/3} + \frac{4\mathcal{M}}{3}\right]\Psi(0) \tag{4.2a}$$

$$Z'(a) + 2\mathcal{M}\gamma^2\eta_1(a) = 0, \quad Z(a) = 2\mathcal{M}\left[\eta_1'(a) + \Psi(a)\right] \quad \text{and}$$

$$Z(a) = \left(1 + \frac{4\mathcal{M}}{3}\right)\Psi(a) + Q\eta_1(a), \tag{4.2b}$$

$$\int_0^a |Z|^2 + |\Psi|^2 + |\eta_1|^2 + \gamma^{-2}\left|\Psi + \eta_1'\right|^2 \,\mathrm{d}z = 1. \tag{4.2c}$$

The dimensionless flow rate is independent of depth, and can be computed through taking its value at $z = a$ where $\Phi_0 = 1$,

$$Q = \left(1 + \frac{4\mathcal{M}}{3}\right)\Phi_0'(a). \tag{4.3}$$

4.1. *Horizontal banding ($\gamma = 0$) instability of the steady state*

We first consider the simpler problem of the stability of the steady state that we have calculated to planar compaction-like profiles with $\gamma = 0$. Combining equation (4.1*a*) with the surface boundary condition (4.2*b*) shows that Z is a constant in this case. Furthermore, equation (4.1*b*) combined with basal boundary conditions (4.2*a*) implies that $\Psi = -\eta_1'$ and therefore that $Z \equiv 0$.

The reduced stability problem with $\xi_\parallel = 0$ and $\gamma = 0$ is

$$\left(\frac{4\mathcal{M}}{3} + \Phi_0^{\frac{2}{3}}\right)\eta_1'''(z) = \left[s\Phi_0^{\alpha-\frac{1}{3}} - \frac{1}{3}\alpha Q\Phi_0^{\alpha-\frac{4}{3}}\Phi_0' - \frac{4}{9}\Phi_0^{-\frac{4}{3}}\Phi_0'^2 - \frac{2}{3}\Phi_0^{-\frac{1}{3}}\Phi_0''\right]\eta_1'(z) +$$

$$\left[\alpha Q\Phi_0^{\alpha-\frac{1}{3}} - \frac{4\mathcal{M}}{3}\Phi_0^{-1}\Phi_0' - \frac{7}{3}\Phi_0^{-\frac{1}{3}}\Phi_0'\right]\eta_1''(z) - s\Phi_0^{\alpha-\frac{4}{3}}\Phi_0'\eta_1(z) \quad \text{with} \tag{4.4a}$$

$$\eta_1(0) = \eta_1'(0) = 0, \quad \left(1 + \frac{4\mathcal{M}}{3}\right)\eta_1'(a) = Q\eta_1(a); \quad \int_0^a \left|\eta_1'\right|^2 + |\eta_1|^2 \,\mathrm{d}z = 1. \tag{4.4b}$$

This can be solved numerically (see appendix C for details on the numerical technique) to find the growth rate of planar instabilities. Figure 5 shows the variation of s with $\mathcal{P}$ and $\mathcal{M}$ for a number of different values of α. It can be calculated that there is no instability when $\alpha = 0$, but for larger values of α, situations where there is more compaction (i.e. $\mathcal{P}$ is higher and $\mathcal{M}$ is lower), the steady states calculated above may well never be reached, since they are unstable to perturbations with no horizontal variation.

The mechanism for this instability depends entirely on the fact that swelling creates a more permeable gel. Figure 6 shows the case of a growing instability, illustrating how there is compaction near $z = a$ and swelling closer to the base. This drives an instability since the compacted layer, with its lower permeability, 'shields' the bulk of the gel layer from the large fluid pressure load, allowing it to swell as a result. This, in turn, concentrates more of the overall pressure drop into the compacted region near $z = a$ and allows for more swelling in the bulk.

Any instability is resisted by diffusive behaviours, with water being driven from swollen regions to less swollen ones, which acts to stabilise. Furthermore, if the matrix is sufficiently stiff, the reconfiguration that results in an instability will be resisted by anchoring from the base, which remains undeformed. In order for the situation to be unstable, there must be a strong enough dependence of permeability on polymer fraction so that the mechanism outlined above can redistribute loads on the gel into a compacted surface layer. This requires

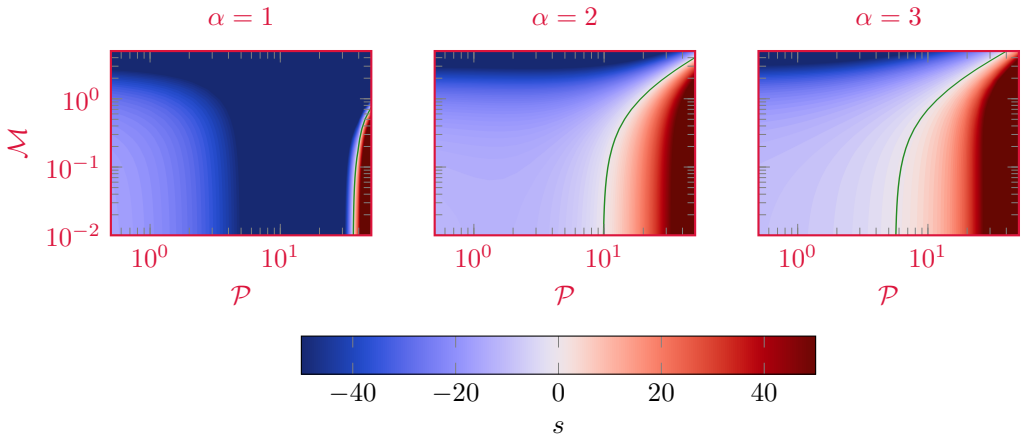


Figure 5: Plots of the growth rate s for instabilities with zero wavenumber, showing how the base state is unstable to 'horizontal banding' modes if the stiffness is low enough (i.e. $\mathcal{M}$ is low) and the pressure head is sufficiently high. The stability decreases as α is increased.

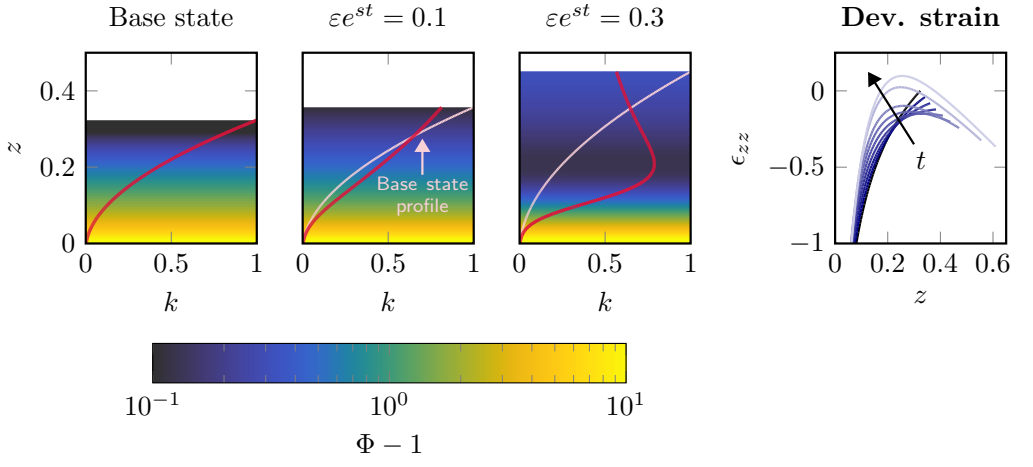


Figure 6: Exaggerated plots of a growing compaction instability where $\gamma = 0$, $\mathcal{M} = 0.1$, $\mathcal{P} = 20$ and $\alpha = 2$, illustrating a mechanism swelling the lower part of the gel and compacting its surface. At each time step, the permeability through the gel is plotted. Though we expect linear theory not to hold for such large perturbation amplitudes, this illustrates clearly how such an instability could grow, through relieving deviatoric strains present in the base state, as seen in the right-hand panel.

a sufficiently large value of α. In figure 7, it is shown that the critical value of α above which instability is seen depends on $\mathcal{P}$ and $\mathcal{M}$ but is apparently never below $\alpha = 4/13$, and so the driving process behind this instability is entirely fluid-mechanical, modified by the solid mechanics of the base state and the deformation needed to accommodate the perturbed state. The limit $\alpha = 4/13$ in the absence of shear ($\mathcal{M} \to 0$) and with extreme loading ($\mathcal{P} \to \infty$) is calculated in appendix B.

In purely elastic problems, wrinkling and other forms of instability occur because the deformed physical state is energetically favourable; it is a lower-energy state than the undeformed base state (Timoshenko & Gere 1961). In our case, there are also energetic

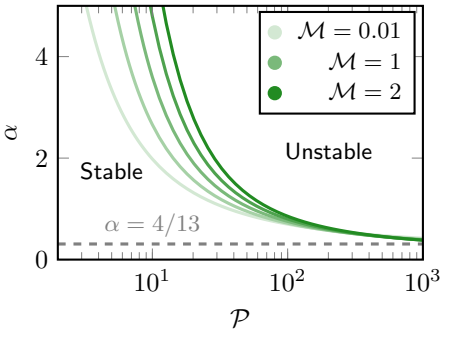


Figure 7: Plots of the critical value of α above which an instability can be triggered for a variety of values of $\mathcal{P}$ and $\mathcal{M}$, showing that there is never an $\alpha = 0$ instability. The calculated analytic limit for instability in the zero-$\mathcal{M}$ and high-$\mathcal{P}$ limit, $\alpha = 4/13$, is plotted as a dashed line.

contributions arising from the fluid phase and its interactions with the polymer scaffold, which are encapsulated by the pervadic and osmotic pressures. Even when swelling and deswelling flows are explicitly considered, it has been shown that elasticity will dominate in the formation of wrinkle or crease instabilities (Webber & Worster 2024). The choice of specific energy density function for a two-phase poroelastic material will change the criterion for a banded state to be energetically favourable, and our strong formulation of this problem in terms of constitutive stress–strain relations (as opposed to energy density–strain constitutive laws) mean that the exact energy density function that corresponds to the problem we solve here cannot be determined (Webber & Montenegro-Johnson 2025). However, a qualitative interpretation for the deformed state corresponding to a lower-energy situation can be seen in figure 5; growing the perturbation leads to a reduction in the total deviatoric stress, reducing the stored elastic energy. Unlike in studies of wrinkling, however, the key difference in the present work is that the driving mechanism is purely differential swelling and not elastically-driven, showing that instabilities are possible provided $\alpha \gtrsim 0.308$, which is true for many reported values in the literature (Etzold *et al.* 2021; Feng *et al.* 2026).

Material parameters other than α vary the stability properties to a lesser extent. Firstly, the hydraulic pressure difference across the gel $\mathcal{P}$ must be sufficiently large to drive the mechanism outlined above, introducing enough compaction into the base state so as to require relief and form a deswollen shield. The stiffness parameter $\mathcal{M}$ cannot be so large as to make differential compaction, introducing gradients in polymer fraction, difficult. Furthermore, larger stiffnesses introduce less compaction for the same driving pressure $\mathcal{P}$, lowering the instability of the base state. Therefore, increasing $\mathcal{M}$ stabilises the compaction instability – this case where changing one parameter has effects on the stability through both modifying the base state *and* the mechanism by which instability occurs, making it difficult to tease out the dominant process, will be a recurring theme in this study.

4.2. *Channelling instability*

If we instead consider $\gamma \neq 0$, we can solve the complete set of equations (4.1) alongside conditions (4.2) to show that channel-like instabilities can form as well as those with $\gamma = 0$. Indeed, these may sometimes be favourable, since the vertical lengthscale of a horizontal banding instability is by necessity a, so anchoring from the base may well stabilise the situation. In cases where γ is larger than $1/a$, a new shorter lengthscale is introduced and deformation need only occur to a smaller depth in the gel. As $\gamma \to \infty$, all instability is smoothed out diffusively, since the lengthscale of the wrinkle-like perturbations is sufficiently

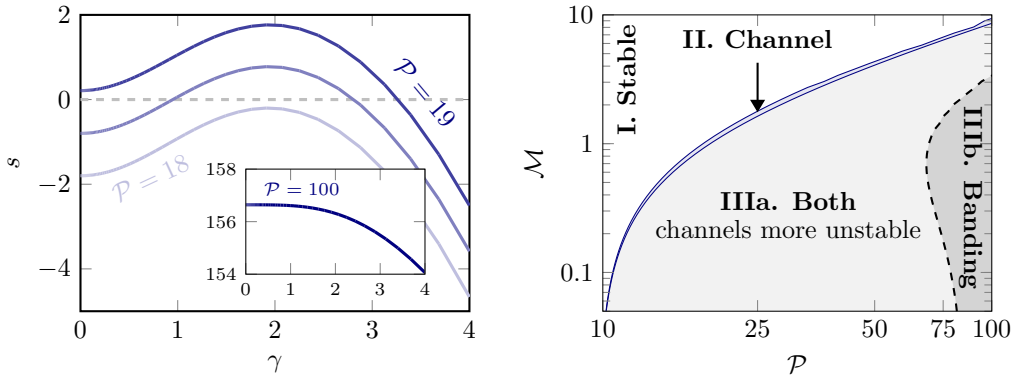


Figure 8: On the left, plots of the instability growth rate against wavenumber γ for different values of $\mathcal{P} = 18, 18.5, 19, 100$ when $\mathcal{M} = 1$. Notice how the most unstable mode at $\gamma = \gamma^*$ suggests a finite-wavenumber instability for all but the $\mathcal{P} = 100$ case. On the right, a phase diagram showing the four distinct types of stability for different values of $\mathcal{P}$ and $\mathcal{M}$. In both cases, $\alpha = 2$.

small as to immediately restabilise through the transport of water from dried to swollen regions. Furthermore, forming very small wavelength wrinkles on the surface of the gel is unfavourable since it generates large amounts of shear.

On the other hand, longer-wavelength disturbances can also be unfavourable since a greater horizontal lengthscale requires displacement deeper into the compacted gel, and the anchored base resists this deformation. As such, in many cases, we expect there to be an intermediate wavenumber γ^* where the instability grows fastest, corresponding to the distance between successive 'channels' that we expect to see in reality. Figure 8 shows some examples where $\alpha = 2$ and $\mathcal{M} = 1$ that illustrate distinct behaviours, namely:

Type I: no horizontal banding with $\gamma = 0$ *and* no channelling instability with $\gamma > 0$
In this case, there is not enough of a driving compaction to trigger an instability of any kind, and $s(\gamma) < 0$ for all γ. This is the case when the layer is insufficiently compacted to create a shielding effect, and is thus found when $\mathcal{P}$ is small or $\mathcal{M}$ is large.

Type II: no horizontal banding with $\gamma = 0$ *but* channelling for finite values of γ
In this case, there is enough deviatoric stress in the compacted base state to trigger relief by channel-like swelling for a finite range of wavelengths, not including the limit of infinite wavelength, a banding instability. Therefore, only a channelling instability will form. This occurs for intermediate values of $\mathcal{P}$, as evident in the middle, $\mathcal{P} = 18.5$, case of figure 8, but is a comparatively small region in parameter space, as seen on the phase diagram.

Type IIIa: horizontal banding with $\gamma = 0$ *and* a preferred channelling instability for finite values of γ (maximum growth rate at $\gamma^* > 0$)
Here, both horizontal banding and channelling are permitted, but the maximum growth rate occurs at a finite $\gamma = \gamma^*$, so we expect to see a channelling instability.

Type IIIb: preferred horizontal banding instability with $\gamma = 0$ *and* potential channelling instability $\gamma > 0$
In this case, seen when $\mathcal{P}$ is especially high (for example, the $\mathcal{P} = 100$ inset in figure 8), the system is again unstable to perturbations for a range of values of $\gamma \geqslant 0$, but the highest

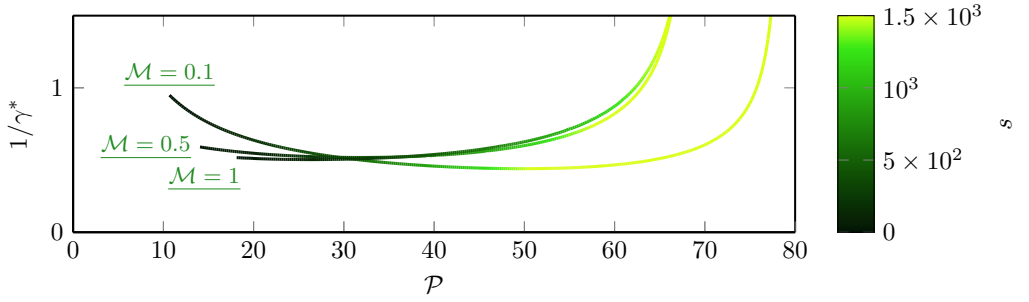


Figure 9: Plots of the most unstable 'wavelength' $1/\gamma^*$ for an instability as the pressure $\mathcal{P}$ is increased for a variety of different stiffnesses $\mathcal{M}$. Also shown is the growth rate s, illustrating how this increases with $\mathcal{P}$. This plot shows how there is initially no instability up to a critical $\mathcal{P}$, beyond which the wavelength of channels drops before growing unboundedly to a point where only compaction or 'banding' instability is seen. For each plot, $\alpha = 2$.

growth rate is at $\gamma = 0$, so we expect to see a horizontal banding instability.

If the pressure is increased across a layer of gel, therefore, there will initially be no instability (type I), followed by the onset of channelling with a finite wavenumber γ^*, corresponding to instabilities of types II and then IIIa. Eventually, the increase in pressure will compact the gel sufficiently that its depth is small and only compaction-type horizontal banding instabilities will be seen, since the highest growth rates are at $\gamma = 0$ (type IIIb). In effect, this can be seen by following a horizontal line across the phase plot in figure 8.

Figure 9 plots γ^* against $\mathcal{P}$, showing also the growth rate of the instability at $\gamma = \gamma^*$. As would be expected, a higher pressure is required to trigger instability as $\mathcal{M}$ rises, owing to the greater cost of deforming the base state with more stiffness. Figure 8 shows that the boundary between regions IIIa and IIIb is not monotonic in $\mathcal{M}$, with the competing effects of greater stiffness resisting the formation of long-wavelength instabilities (stresses build due to the anchored base) and greater stiffness working against the formation of small surface wrinkles (shear stresses build close to the surface) working in opposite directions. In the case of figure 9, increasing $\mathcal{M}$ leads to a transition to type IIIb instability at a smaller loading pressure for this latter reason.

Much as with the horizontal banding case, parameters α and $\mathcal{M}$ will affect the quantitative properties of the instability, but teasing out whether these effects result from differences in the base state or in the physics driving the growth of unstable states is more challenging. The results of varying $\mathcal{M}$ suggest that much of the qualitative effect of changing the stiffness arises from less compression in the base state when the gel is stiffer, since the most unstable mode becomes shorter-wavelength with increasing stiffness – the opposite effect to what would be expected from increasing stiffness, which would smooth out small 'wrinkles'.

In figure 11, the nature of the perturbation swelling is plotted for a range of different values of α. The pressure head $\mathcal{P}$ and the stiffness parameter $\mathcal{M}$ are kept the same for all three plots. These plots allow us to notice the mechanisms that set the lengthscale of the most unstable mode and what effect this will have, qualitatively, in systems where water is driven through a gel. First, realise that the wavelength for an instability typically increases with α, and this is because the amount of compaction decreases with α for the same overpressure. Hence, the only lengthscale in the problem – the thickness of the gel layer – is greater, giving larger spacing between adjacent regions of swelling. Furthermore, deformation is very much localised to the compacted base of the gel as α is increased. Returning to figure 3, this is to

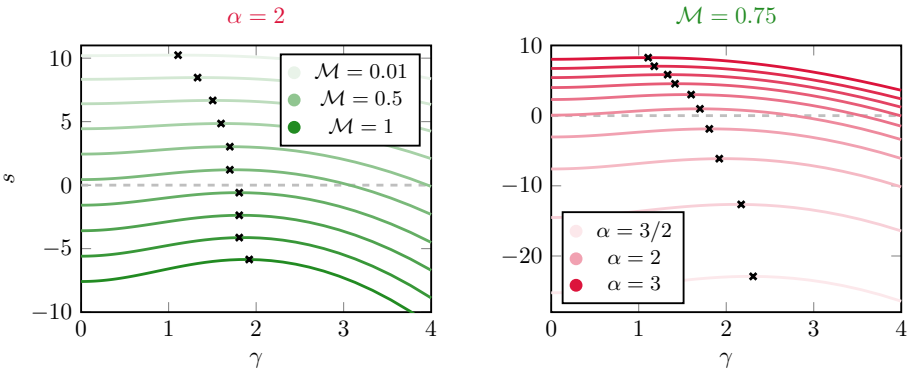


Figure 10: On the left, the influence of changing $\mathcal{M}$ on the dispersion relation for an instability at fixed α, whilst on the right the influence of changing α whilst holding $\mathcal{M}$ fixed is shown. In either case, the most unstable wavenumber γ^* is marked with a cross. For both plots, $\mathcal{P} = 15$.

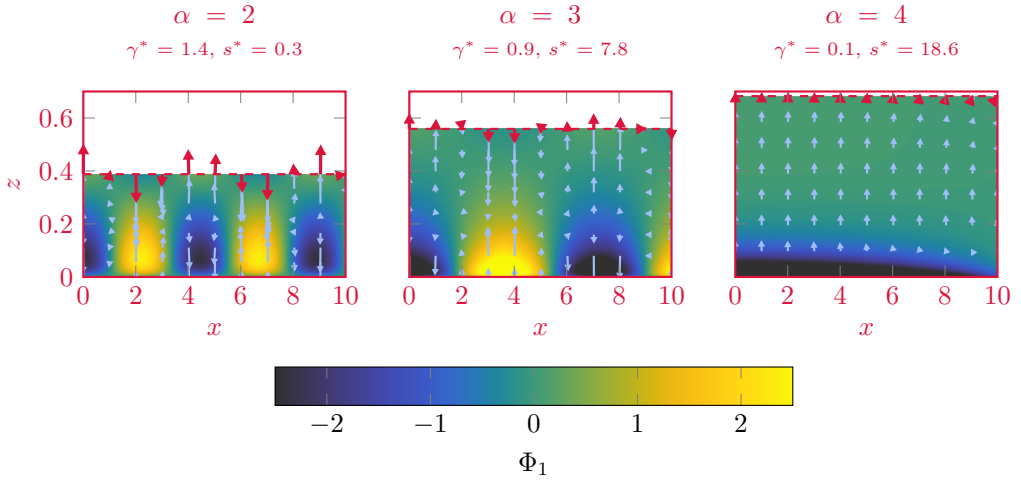


Figure 11: Plots with $\mathcal{P} = 12$ and $\mathcal{M} = 0.25$ illustrating the most unstable eigenmodes with wavenumber γ^* and growth rates s^* for a variety of values of α, showing the swelling and drying that takes place. In blue, the interstitial perturbation fluid velocity, with the red arrows showing the perturbation flux of fluid at the uppermost gel–water interface.

be expected, since deformation localises at the base for larger values of α. Eventually, the most unstable mode corresponds to horizontal banding.

Finally, the plots of the perturbation surface fluid flow illustrate the qualitative presentation of channelling instabilities as they form: water preferentially flows in ‘channels’ spaced by a dimensionless distance $2\pi/\gamma^*$. Eventually, outside of the linear stability region, regions of high stress will form where there is significant swelling, and we expect this eventually to lead to fracture or rupture; either in the form of permanent, open conduit channels (when the linear instability is of channelling form), or those parallel to the base (when the linear instability is horizontal banding).

5. Conclusion

Flow-induced compaction is a complex process where three material properties set the non-trivial response of a poroelastic material to a hydrostatic pressure head. The first two properties – the dependence of isotropic stress on local solid fraction and the dependence of permeability on solid fraction – have been studied in previous work and are responsible for the general form of the compaction profile (denser at the base, uncompacted at the top) and the fact that compression reduces the effective permeability of layers to flow, respectively. In this work, we have considered the effects of a further material property unique to 'cohesive' poroelastic media where the elastic matrix is connected via cross-linking to give a resistance to shear. In all of the cases considered here, this effect is encapsulated by the shear parameter $\mathcal{M}$, which, in effect, measures the matrix's resistance to anisotropic deformation relative to its resistance to isotropic deformation.

The very nature of compaction creates compression profiles that are anisotropic, and the requirement that the top surface of the material remains 'fully swollen' (a side-effect of requiring stress continuity at this boundary) means that increasing the driving force of compaction generates increased shear stresses. Thus, stiffer materials are seen to compact less under the same forcing, but the effect this has on interstitial flows is not as straightforward. For a fixed hydrostatic pressure head, increasing the stiffness $\mathcal{M}$ can either lead to a greater or lesser flux of water through the compacted layer, dependent on whether the resultant increase in permeability (from lower compaction) wins out over the increased thickness of gel providing viscous resistance.

In addition to these complex fluid-mechanical behaviours enabled by considering the influence of shear stresses on compacted media, the relationship between solid fraction and permeability can introduce a new mechanism by which the bulk of the gel is shielded from pressure drops, and instabilities can result. In section 3, it was shown that these can form in two distinct ways, which, though morphologically distinct, arise for the same reason; preferably swelling certain regions results from a shielded deswollen region reducing the loading on the bulk. This can occur either in the form of swelling a region in the middle of a compacted layer, and deswelling its interface with water (horizontal banding) or through swelling preferential 'channels' through which fluid flow is driven faster. It is reasonable to assume that longer-time nonlinear evolution of such states leads to the formation of swollen channels that transport fluid with much less resistance, as are familiar from a number of culinary and geophysical applications. In section 3, a linear stability analysis was carried out that showed how shear is key to the mechanism behind this instability, and how a balance between the deformation lengthscale set in the compacted base state and stabilising diffusion sets the characteristic lengthscale over which these channels can be expected to be seen. Perhaps most interestingly, as the pressure difference across a compacted layer is increased, the preferred mechanism of instability changes from unconditional stability to channelling to eventual horizontal banding alone.

Acknowledgements. JJW thanks Duncan Hewitt (University of Cambridge) for discussions in spring 2024 that led to the problem of channelling outlined in this paper and Ellen Jolley and Danny Booth (University of Warwick and University College London, respectively) for their help in bringing the problem closer to a solution!

For the purpose of open access, the author has applied a Creative Commons Attribution (CC-BY-NC-ND) licence to any Author Accepted Manuscript version arising from this submission.

AI usage declaration. Generative (or other) AI tools were not used anywhere in the development of theory, interpretation, code or writing of this research. Any errors in methodology and presentation are the author's own.

Funding. This work was partly supported by the Leverhulme Trust Research Leadership Award 'Shape-

Transforming Active Microfluidics' (RL-2019-014) to Thomas D. Montenegro-Johnson at the University of Warwick, on which JJW was employed as a postdoctoral research fellow prior to September 2026.

Declaration of interests. The authors report no conflict of interest.

Data availability statement. The raw MATLAB code used to generate the figures in this manuscript is available at https://doi.org/10.5281/zenodo.23413849.

Author ORCIDs. J. J. Webber, https://orcid.org/0000-0002-0739-9574

Appendix A. Analytic solution for the base state as $\mathcal{M} \to \infty$

In the stiff limit $\mathcal{M} \to \infty$, any appreciable compaction can only occur if $\mathcal{P} \sim \mathcal{M}$. Otherwise, the stiffness of the matrix completely resists deformation. In the distinguished limit where this is the case and yet $\Phi \ll \Phi_C$ (i.e. the pressure head is not sufficiently high to completely dewater the gel), osmotic effects become unimportant and the pressure drop relation (2.14) implies that

$$\Phi|_{z=0} \approx \left(1 + \frac{\mathcal{P}}{4\mathcal{M}}\right)^3. \tag{A 1}$$

Furthermore, the governing equation implies that

$$\frac{\partial}{\partial z}\left[\frac{4\mathcal{M}}{3}\Phi^{-(\alpha+2/3)}\frac{\partial \Phi}{\partial z}\right] \approx 0 \quad \text{or} \quad \Phi^{1/3-\alpha} = c_1 z + c_2, \tag{A 2}$$

for constants c_1 and c_2. Forcing $\Phi = 1$ on $z = a$ and $\Phi = \left(1 + \frac{\mathcal{P}}{4\mathcal{M}}\right)^3$ on $z = 0$ gives

$$\Phi = \left\{\left(1 + \frac{\mathcal{P}}{4\mathcal{M}}\right)^{1-3\alpha} + \left[1 - \left(1 + \frac{\mathcal{P}}{4\mathcal{M}}\right)^{1-3\alpha}\right]\frac{z}{a}\right\}^{\frac{3}{1-3\alpha}}. \tag{A 3}$$

Integrating this from $z = 0$ to $z = a$ fixes a to be

$$a = \frac{4-3\alpha}{1-3\alpha}\frac{1 - \left(1 + \frac{\mathcal{P}}{4\mathcal{M}}\right)^{1-3\alpha}}{1 - \left(1 + \frac{\mathcal{P}}{4\mathcal{M}}\right)^{4-3\alpha}}. \tag{A 4}$$

via the constraint of equation (2.10*b*). This permits us to compute the interstitial pressure-driven fluid flux,

$$Q = -\frac{4\mathcal{M}}{4-3\alpha}\left[\left(1 + \frac{\mathcal{P}}{4\mathcal{M}}\right)^{4-3\alpha} - 1\right]. \tag{A 5}$$

This solution loses validity if osmotic effects are important, so when $\mathcal{P} \gtrsim 4\mathcal{M}\Phi_C^{1/3}$. Note that, when $\alpha < 1$, the magnitude of fluxes decreases with increasing stiffness, but if $\alpha > 1$, more stiffness leads to more flow.

Appendix B. Analytic solution for the base state in the low stiffness limit $\mathcal{M} \to 0$

If shear stiffness is insignificant in the mechanics of the poroelastic layer, we can derive a tractable analytic solution in the case of a linear osmotic pressure (i.e. the $\Phi_C \gg 1$ limit of appendix A) where $\Pi(\Phi) = \Phi - 1$. In this case, the polymer fraction on the base of the gel is given by a simplified form of equation (2.14) that shows $\Phi(0) = 1 + \mathcal{P}$. Making the same

assumptions reduces equation (2.10) to

$$\frac{\partial^2}{\partial z^2}\left(\Phi^{1-\alpha}\right) = 0 \quad \text{so} \quad \Phi = \left[\frac{z}{a} + (1+\mathcal{P})^{1-\alpha}\left(1-\frac{z}{a}\right)\right]^{1/(1-\alpha)}, \tag{B 1}$$

on the assumption that $\alpha \neq 1$ (this case is treated explicitly in equation (2.17)). Integrating to find the thickness of the layer, a,

$$a = \frac{2-\alpha}{1-\alpha}\frac{(1+\mathcal{P})^{1-\alpha}-1}{(1+\mathcal{P})^{2-\alpha}-1}. \tag{B 2}$$

In this case, the transport flux Q is simply given by evaluating $\partial\Phi/\partial z$ on the surface $z = a$, so

$$Q = -\frac{(1+\mathcal{P})^{2-\alpha}-1}{2-\alpha}. \tag{B 3}$$

This approximate solution allows us to deduce the minimum value of α that triggers a planar, horizontal banding, instability. Since $\mathcal{M}$ only serves to stabilise any banding, the critical stability threshold for equation (4.4) is crossed in the $\mathcal{M} = 0$ limit. Taking this limit and rewriting $Q = \Phi_0^{-\alpha}\Phi_0'$, these equations reduce to

$$\eta_1''' = Q\left(\alpha - \frac{7}{3}\right)\Phi_0^{\alpha-1}\eta_1'' - \frac{13Q^2\alpha}{9}\Phi_0^{2(\alpha-1)}\eta_1';\ \eta_1(0) = \eta_1'(0) = 0;\ \eta_1'(a) = Q\eta_1(a). \tag{B 4}$$

Now, using the solution (B 1) for Φ_0, change variables to

$$u = \Phi_0^{1-\alpha} = (1+\mathcal{P})^{1-\alpha} - \frac{1-\alpha}{2-\alpha}\left[(1+\mathcal{P})^{2-\alpha}-1\right]z. \tag{B 5}$$

Hence, $\partial/\partial z = (1-\alpha)Q\,\partial/\partial u$, using expression (B 3) for the flux Q. This reduces the governing equation to

$$f_{uuu} = \frac{\alpha - 7/3}{1-\alpha}u^{-1}f_{uu} - \frac{13\alpha}{9(1-\alpha)^2}u^{-2}f_u, \tag{B 6}$$

where $\eta_1(z) = f(u)$. This is an equidimensional differential equation, and we can thus rescale the variable u once more to $v = (u-1)/\left[(1+\mathcal{P})^{1-\alpha}-1\right]$, mapping the upper and lower boundaries to $v = 0$ and $v = 1$, respectively. Hence, on the assumption of no repeated roots ($\alpha \neq 4/13$),

$$f = c_1 + c_2 v^{\frac{1}{3(\alpha-1)}\left[3\alpha-1+\sqrt{4-13\alpha}\right]} + c_3 v^{\frac{1}{3(\alpha-1)}\left[3\alpha-1-\sqrt{4-13\alpha}\right]}, \tag{B 7a}$$

where the c_i are constants, with boundary conditions

$$f(1) = f'(1) = 0 \quad \text{and} \quad f(0) = \frac{1-\alpha}{(1+\mathcal{P})^{1-\alpha}-1}f'(0). \tag{B 7b}$$

Applying these boundary conditions shows that a nonzero solution can only exist in the limit $\alpha \to 4/13$, where f instead takes the form

$$f = c_1 + (c_2 + c_3 \ln v)v^{1/27}, \tag{B 8}$$

and applying boundary conditions at $v = 1$ determines c_1 and c_2. At $v = 0$, we find a surface boundary condition that can only be approached in the large-$\mathcal{P}$ limit (though never satisfied exactly);

$$\frac{v^{-26/27}\ln v}{(1+\mathcal{P})^{9/13}-1} \to 1053 \quad \text{as } v \to 0. \tag{B 9}$$

This explains the large-$\mathcal{P}$ limit of critical α for banding instability, seen to be approximately $4/13 \approx 0.308$ when $\mathcal{M}$ is increasingly small, yet finite.

Appendix C. Numerical solution of the stability equations

To solve the systems of perturbation equations, both in the $\gamma = 0$ case (equations (4.4)) and the $\gamma > 0$ case (equations (4.1)), we start by rescaling the domain from $0 \leqslant z \leqslant a$ to $0 \leqslant y \leqslant 1$ where $y = z/a$. The equations and boundary conditions are unchanged in their form, provided that γ and s are replaced by

$$s_N = a^2 s \quad \text{and} \quad \gamma_N = a\gamma, \tag{C 1}$$

and the arbitrary normalisation (4.2*c*) remains an integral equal to unity in the new variables.

The equations (4.4) are first solved using `bvp5c` in MATLAB to provide an initial guess for the solution of equations (4.1), ensuring that the solutions remain on the same desired branch. To ensure convergence, the solution is continued along increasing values of γ, with the solution $(\hat{Z}, \hat{\Psi}, \hat{\eta}_1)$ used as an initial guess for the next value of γ, replacing the normalisation condition (4.2*c*) with

$$\int_0^1 Z\hat{Z} + \Psi\hat{\Psi} + \eta_1\hat{\eta}_1 + \gamma^{-2}(\Psi + \eta_1')(\hat{\Psi} + \hat{\eta}_1')\,\mathrm{d}y = 1. \tag{C 2}$$

This prevents the structure of the eigenfunctions changing significantly when values of γ only change a small amount. Then, when a normalised solution is required, it can be normalised with condition (4.2*c*) using this solution as an initial guess.

REFERENCES

Biot, M. A. 1941 General theory of three-dimensional consolidation. *J. Appl. Phys.* **12**, 155–164.

Bouckley, E. R., Sourcis, B. & Hewitt, D. R. 2025 The interplay of flow-induced, gravitational and mechanical compaction in soft porous media. *J. Fluid Mech.* **1018**, A26.

Coussy, O. 2004 *Poromechanics*. Wiley.

Dhopeshwarkar, R., Crooks, R. M., Hlushkou, D. & Tallarek, U. 2008 Transient effects on microchannel electrokinetic filtering with an ion-permselective membrane. *Anal. Chem.* **80**, 1039–1048.

Drazin, P. G. & Reid, W. H. 2004 *Hyrodynamic Stability (2nd edn.)*. Cambridge University Press.

Etzold, M. A., Linden, P. F. & Worster, M. G. 2021 Transpiration through hydrogels. *J. Fluid Mech.* **925**, A8.

Feng, Y., Gerber, D., Heyden, S., Kröger, M., Dufresne, E. R., Isa, L. & Style, R. W. 2025 Characterizing hydrogel behavior under compression with gel-freezing osmometry. *J. Mech. Phys. Solids* **201**, 106166.

Feng, Y., Jung, S.-H., Sirvinksi, C., Balkanyi, D., Paratore, F., Isa, L. & Style, R. W. 2026 Extracting hydrogel properties by watching hydrogel particles moving through solid ice. *arXiv preprint* **physics.cond-mat.soft**, 2609.29904.

Ghosh, M. V., Hennessy, M. G., Münch, A. & Waters, S. L. 2026 Modelling flow-driven pore closure of weakening poroelastic media. *arXiv preprint* **physics.flu-dyn**, 2608.17581.

Godard, Z. C., Moulton, D. E. & Waters, S. L. 2025 Cyclic loading of a heterogeneous non-linear poroelastic material. *Soft Matter* **21**, 7487–7507.

Golfier, F., Zarcone, C., Bazin, B., Lenormand, R., Lasseux, D. & Quintard, M. 2002 On the ability of a Darcy-scale model to capture wormhole formation during the dissolution of a porous medium. *J. Fluid Mech.* **457**, 213–254.

Hewitt, D. R., Nijjer, J. S., Worster, M. G. & Neufeld, J. A. 2016 Flow-induced compaction of a deformable porous medium. *Phys. Rev. E* **93**, 023116.

Lee, W. T., Smith, A. & Arshad, A. 2023 Uneven extraction in coffee brewing. *Phys. Fluids* **35**, 054110.

Lentle, R. G., Janssen, P. W. M. & Hume, I. D. 2009 The roles of filtration and expression in the processing of digesta with high solid phase content. *Comp. Biochem. Physiol. A* **154**, 1–9.

Lu, X. L. & Mow, V. C. 2008 Biomechanics of articular cartilage and determination of material properties. *Med. Sci. Sports Exerc.* **40**, 193–199.

MacMinn, C. W., Dufresne, E. R. & Wettlaufer, J. S. 2015 Fluid-driven deformation of a soft granular material. *Phys. Rev. X* **5**, 011020.

MacMinn, C. W., Dufresne, E. R. & Wettlaufer, J. S. 2016 Large deformations of a soft porous material. *Phys. Rev. Appl.* **5**, 044020.

Minale, M. 2014 Momentum transfer within a porous medium. II. Stress boundary condition. *Phys. Fluids* **26**, 123102.

Morgan, M. L., James, D. W., Monloubou, M. & Sandnes, B. 2025 Wormhole formation in fluid-driven granular flow. *Commun. Phys.* **8**, 468.

Paterson, D. T., Eaves, T. S., Hewitt, D. R., Balmforth, N. J. & Martinez, D. M. 2019 Flow-driven compaction of a fibrous porous medium. *Phys. Rev. Fluids* **4**, 074306.

Peppin, S. S. L., Elliott, J. A. W. & Worster, M. G. 2005 Pressure and relative motion in colloidal suspensions. *Phys. Fluids* **17**, 053301.

Song, R., Stone, H. A., Jensen, K. H. & Lee, J. 2019 Pressure-driven flow across a hyperelastic porous membrane. *J. Fluid Mech.* **871**, 742–754.

Terzaghi, K. 1925 *Erdbaumechanik: auf bodenphysikalischer Grundlage*. F. Deuticke.

Timoshenko, S. P. & Gere, J. M. 1961 *Theory of Elastic Stability, 2nd edition*. McGraw-Hill.

Waszkiewicz, R., Myck, F., Białas, Ł., Puciata-Mroczynska, M., Dzikowski, M., Szymczak, P. & Lisicki, M. 2025 Under pressure: poroelastic regulation of flow in espresso brewing. *arXiv preprint* **physics.flu-dyn**, 2512.21528.

Webber, J. J., Etzold, M. A. & Worster, M. G. 2023 A linear-elastic-nonlinear-swelling theory for hydrogels. Part 2. Displacement formulation. *J. Fluid Mech.* **960**, A38.

Webber, J. J. & Montenegro-Johnson, T. D. 2025 Poromechanical modelling of responsive hydrogel pumps. *J. Fluid Mech.* **1009**, A38.

Webber, J. J. & Worster, M. G. 2023 A linear-elastic-nonlinear-swelling theory for hydrogels. Part 1. Modelling of super-absorbent gels. *J. Fluid Mech.* **960**, A37.

Webber, J. J. & Worster, M. G. 2024 Wrinkling instabilities of swelling hydrogels. *Phys. Rev. E* **109**, 044602.

Webber, J. J. & Worster, M. G. 2025 Cryosuction and freezing hydrogels. *Proc. Roy. Soc. A* **481**, 20240721.

Xu, Z., Zhang, J., Young, Y.-N., Yue, P. & Feng, J. J. 2022 Comparison of four boundary conditions for the fluid-hydrogel interface. *Phys. Rev. Fluids* **7**, 093301.

Yang, S., Gerber, D., Feng, Y., Bain, N., Kuster, M., de Lorenzis, L., Xu, Y., Dufresne, E. R. & Style, R. W. 2024 Dehydration drives damage in the freezing of brittle hydrogels. *Sci. Adv.* **10**, eado7750.